LI, F. H. (1987). *Acta Cryst.* **A43**, C247.
LI, F. H. & TANG, D. (1985). *Acta Cryst.* **A41**, 376-382.
LYNCH, D. F., MOODIE, A. F. & O'KEEFE, M. A. (1974). *Abstr. 8th Int. Congr. Electron Microsc. Electron Microscopy* 1974, edited by J. M. SANDERS & D. J. GOODCHILD, pp. 222-223. Canberra: Australian Academy of Science.
LYNCH, D. F. & QIN, L. C. (1987). *J. Appl. Cryst.* **20**, 442-444.
MEGAW, H. D. (1973). *Crystal Structures: a Working Approach*, p. 286. Philadelphia, PA: W. B. Saunders.
OLSEN, A. (1983). *Collected Abstracts. 14th Meet. Soc. Crystallogr. Aust., Morpeth, Australia.* The Society of Crystallographers in Australia.
OLSEN, A., GOODMAN, P. & MCLEAN, D. J. (1983). *Proc. 41st Meet. EMSA*, edited by G. W. BAILEY, pp. 40-41. San Francisco Press.

Acta Cryst. (1988). A**44**, 912-927

Visibility of Single Heavy Atoms on Thin Crystalline Silicon in Simulated Annular Dark-Field STEM Images

BY RUSSELL F. LOANE, EARL J. KIRKLAND AND JOHN SILCOX

School of Applied and Engineering Physics, Cornell University, Ithaca, NY 14853, *USA*

(*Received* 30 *November* 1987; *accepted* 25 *May* 1988)

Abstract

The multislice method, pioneered by Cowley and Moodie, has recently been adapted to simulate annular dark-field scanning transmission electron-microscope (ADF STEM) images. This paper presents a series of calculations using this new approach with experimental parameters appropriate for a VG-HB501 STEM to investigate the visibility of single heavy adatoms on thin crystalline silicon membranes. The tendency for electrons to channel along columns of atoms in crystals can greatly increase the intensity incident on an adatom on the exit surface, thereby increasing the adatom visibility. The simulations indicate that an adatom on the exit surface on a column of crystal atoms is up to three times as visible as an adatom on the entrance surface, and that the adatom remains highly visible as the crystal thickness is increased. Tilting the specimen or displacing the adatom from the column appears to lower the visibility of the adatom dramatically. These calculations suggest that, with the appropriate imaging conditions, a single gold adatom may be visible on at least 235 Å of (111) silicon.

1. Introduction

Images of single heavy atoms on very thin amorphous substrates were first produced using annular dark-field scanning transmission electron microscopy (ADF STEM) imaging techniques (Crewe, Langmore & Isaacson, 1975; Isaacson, Langmore, Parker, Kopf & Utlaut, 1976). In this situation, incoherent imaging conditions apply (Cowley, 1976), and a simple physical model in which the intensity scattered from each atom is added together linearly provides a description of the conditions for visibility of the heavy adatom. On crystalline substrates, diffraction can be a significant factor in the ADF signal (Cowley, 1973) and experimental images may be difficult to interpret (Donald & Craven, 1979). This difficulty has led to efforts to minimize dynamical diffraction effects by increasing the inner angle of the detector (Howie, 1979; Treacy, 1981) or by orienting the crystal away from the strong Bragg reflections found at low-order zone axes (Pennycook, Berger & Culbertson, 1986). As yet no experimental observations of single heavy atoms on crystalline substrates with ADF STEM have been reported, though the sensitivities produced to date suggest that one bismuth atom might have a 50% contrast in 270 Å thick silicon (110) crystals (Pennycook *et al.*, 1986).

An advantage of including diffraction in low-order axis imaging is that it may be possible to image the adatom and the crystal simultaneously, allowing the determination of the adatom position with respect to the crystal lattice. The difficulty is the image interpretation. As mentioned above, the response has been to set up experimental conditions to simplify this step, by discarding all crystal-lattice information. An alternative approach is to simulate the images and use the simulations as a guide to interpretation. This latter approach is now standard in conventional transmission electron microscopy (CTEM), and has been followed in this paper for STEM. A series of ADF STEM image simulations of heavy adatoms on thin crystalline silicon (111) films are presented as a guide to possible experimental studies.

Simulations are an essential tool of electron microscopy. Because image formation for crystalline specimens is a complex nonlinear process, simple analytical descriptions are inadequate. Interference effects can lead to significant misinterpretation of results (Engel, Wiggins & Woodruff, 1974). Numerically intensive simulations are necessary as a guide to the

0108-7673/88/060912-16$03.00

correct interpretation. Simulations are used to interpret artifacts in experimental images, to investigate the effects of microscope parameters such as lens defocus, lens spherical aberration, beam tilt, detector geometry *etc.*, to investigate the effects of specimen parameters such as specimen thickness and tilt, and to explore the capabilities of existing or hypothetical microscopes and imaging techniques. The multislice simulation algorithm (Cowley & Moodie, 1957) is one of the most valuable simulations for CTEM. New applications, modifications, and analysis of the algorithm appear regularly (Goodman & Moodie, 1974; Ishizuka & Uyeda, 1977; O'Keefe & Buseck, 1979; Self, O'Keefe, Buseck & Spargo, 1983; Van Dyck, 1985). A recent modification of the algorithm has extended its applicability to include the simulation of ADF STEM images (Kirkland, Loane & Silcox 1987). This first application of the STEM simulation indicated a high visibility for a single platinum atom on 50 Å crystalline silicon. A closer look at single adatom visibility using the STEM simulation is presented in this paper.

Dynamical diffraction near low-order crystal axes can focus an incident electron probe into intense narrow peaks centered on the columns of crystal atoms (Hirsch, Howie, Nicholson, Pashley & Whelan, 1965; Howie, 1966; Kambe, Lehmpfuhl & Fujimoto, 1974; Buxton, Loveluck & Steeds, 1978; Fertig & Rose, 1981). This effect has been used in CTEM to determine the location of impurity atoms in crystals by examining the amount of electron-stimulated characteristic X-ray emissions as a function of the amount of channeling (Spence & Tafto, 1982; Pennycook & Narayan, 1985). In STEM, the channeling peak intensity can be very large (Fertig & Rose, 1981). Such channeling should greatly enhance or reduce the signal from an adatom on the crystal exit surface, depending on whether the adatom is located on a column of crystal atoms or not. The channeling enhancement of the single adatom signal may make single-atom imaging easier to achieve in certain cases on thin crystals than on thin amorphous films.

These ideas raise some questions that can be addressed by simulation. How visible are single heavy adatoms on crystalline silicon under feasible experimental conditions? What is the maximum crystal thickness at which an adatom is still visible? What is the effect of specimen tilt on visibility, and how carefully must the specimen be aligned? How sensitive is visibility to the placement of the adatom on the entrance or exit surface of the crystal? And what is the effect of noise?

This paper is organized in the following way. A summary of the STEM image calculation and the choice of microscope and specimen parameters are given in §§ 2 and 3. Channeling of the electron probe and the effects of specimen thickness, specimen tilt, and probe placement are investigated in § 4. STEM image simulations and the effects on adatom visibility of specimen thickness, specimen tilt, and adatom position are presented in § 5. Finally, the effects of noise on the visibility of the adatoms are given in § 6.

2. The STEM image calculation

In dark-field STEM image formation, a highly focused electron beam is scanned across the specimen and the scattered intensity, integrated over an annular detector, is displayed as a function of the probe position. To simulate such an image, an entire CTEM multislice calculation is performed for each position of the incident probe (Cowley & Spence, 1979). Details of this calculation are given by Kirkland *et al.* (1987), and are summarized here.

The wavefunction of an incident probe, centered at a point $\mathbf{x}_p$ on the specimen surface, can be written as

$$\psi_{\text{inc}}(\mathbf{x}, \mathbf{x}_p) = \int_{\text{all } \mathbf{k}} A(\mathbf{k}) \exp[-2\pi i \mathbf{k} \cdot (\mathbf{x} - \mathbf{x}_p) - iW(\mathbf{k})]\, d\mathbf{k}, \quad (1)$$

where the wavevector $\mathbf{k}$ corresponds to a plane wave propagating at an angle $\alpha = \lambda \mathbf{k}$ to the optical axis. The objective-lens aberration function, $W(\mathbf{k})$, and aperture function, $A(\mathbf{k})$, are defined

$$W(\mathbf{k}) = \pi\lambda k^2 (C_s \lambda^2 k^2/2 - \Delta f) \quad (2)$$

$$A(\mathbf{k}) = A_0\{1 + \exp[(k^2 - k_{\text{ap}}^2)/\delta_{\text{ap}}]\}^{-1}, \quad (3)$$

where C_s is the spherical aberration, Δf is the defocus, and $\alpha_{\text{ap}} = \lambda \mathbf{k}_{\text{ap}}$ is the aperture angle of the objective lens. A_0 is chosen so that the total integrated intensity of the incident beam is unity. Smoothing of the objective aperture by a Fermi function with a width, δ_{ap}, of one pixel was necessary to better describe the relatively small circular aperture on a discretely sampled square array.

The incident probe is then propagated through the crystal by means of the multislice algorithm.

$$\psi_1(\mathbf{x}, \mathbf{x}_p) = t_1(\mathbf{x}) \psi_{\text{inc}}(\mathbf{x}, \mathbf{x}_p) \quad (4)$$

$$\psi_{i+1}(\mathbf{x}, \mathbf{x}_p) = t_{i+1}(\mathbf{x})[\psi_i(\mathbf{x}, \mathbf{x}_p) \otimes p(\mathbf{x})], \quad (5)$$

where $\otimes$ represents a convolution. The transmission functions, $t_i(\mathbf{x})$, in (4) and (5) are defined in terms of the projected potential of the ith slice, $v_i(\mathbf{x})$,

$$t_i(\mathbf{x}) = \exp[iv_i(\mathbf{x})] \otimes m(\mathbf{x}). \quad (6)$$

A low-pass filter, $m(\mathbf{x})$, is necessary to prevent aliasing in the discrete Fourier transforms.

$$m(\mathbf{x}) = \mathcal{FT}^{-1}[M(\mathbf{k})] = \mathcal{FT}^{-1}(\{1 + \exp[(k^2 - k_{\text{lim}}^2)/\delta_{\text{lim}}]\}^{-1}) \quad (7)$$

where $\mathcal{FT}^{-1}$ represents a two-dimensional inverse Fourier transform. The limiting spatial frequency,

$k_{\lim} = \alpha_{\lim}/\lambda$ [which was inadvertently stated incorrectly in the previous paper (Kirkland *et al.*, 1987)], is defined by the slice size in ångströms a_x, b_y and slice sampling in pixels N_x, N_y.

$$k_{\lim} = \tfrac{2}{3} \text{ minimum } (N_x/2a_x, N_y/2b_y). \quad (8)$$

The projected potential of the ith slice in units of radians phase shift of the transmitted electron wavefunction is calculated from a parameterization of X-ray scattering factors (*International Tables for X-ray Crystallography*, 1974) *via* the improved Mott formula (Peng & Cowley, 1988).

$$v_i(\mathbf{x}) = \mathcal{FT}^{-1}\{\gamma\lambda/(a_x b_y 2\pi R_B) \sum_j \exp(2\pi i \mathbf{k}.\mathbf{x}_j) \times \sum_h a_{jh}[1-\exp(-b_{jh}k^2/4)]/k^2\}, \quad (9)$$

where $\gamma = m/m_0$ is the relativistic mass ratio, $R_B = 0{\cdot}529$ Å is the Bohr radius, j ranges over all the atoms in the ith slice, and a_{hj} and b_{hj} are constants in the parameterization of the X-ray scattering factors for a single atom of atomic number Z_j. The propagator function, $p(\mathbf{x})$, in (5) is simplest to define in reciprocal space.

$$p(\mathbf{x}) = \mathcal{FT}^{-1}\{\exp[2\pi i \Delta z(k_x \tan\theta_x + k_y \tan\theta_y - \lambda k^2/2)]M(\mathbf{k})\}, \quad (10)$$

where Δz is the slice thickness, (θ_x, θ_y) is the specimen tilt, and $M(\mathbf{k})$ is the Fourier transform of the antialiasing function defined above.

After passing through the N_z slices of the specimen, the wavefunction is propagated to the detector plane in the far field, and the electron intensity is incoherently integrated over an annulus. The resulting signal, $g(\mathbf{x}_p)$, is the fraction of incident intensity detected as a function of probe position.

$$\Psi_{\text{det}}(\mathbf{k}, \mathbf{x}_p) = \mathcal{FT}[\psi_{N_z}(\mathbf{x}, \mathbf{x}_p)] \quad (11)$$

$$g(\mathbf{x}_p) = \int_{\text{all k}} |\Psi_{\text{det}}(\mathbf{k}, \mathbf{x}_p)|^2 D(\mathbf{k})\, d\mathbf{k}. \quad (12)$$

The detector function is defined as

$$D(\mathbf{k}) = \{1+\exp[(k_{\text{in}}^2 - k^2)/\delta_{\text{in}}]\}^{-1} \times \{1+\exp[(k^2 - k_{\text{out}}^2)/\delta_{\text{out}}]\}^{-1}, \quad (13)$$

where $k_{\text{in}} < k_{\text{out}} \leq k_{\lim}$ defines the range of angles of collected scattered intensity.

Throughout these simulations, real-world complications such as a nonzero source size, thermal vibration, mechanical vibration, stray electromagnetic fields, fluctuations in the accelerating potential, noise in the electronics, *etc.* have been ignored.

3. Specimen and microscope parameters

Before any multislice calculation can be performed, the transmission function for each slice of the simulated specimen must be calculated. Bulk silicon (111) is a layered structure with a 9·4 Å repeat distance. A choice of 9·4 Å thick slices is too large for 100 keV electrons, since it produces an artificial first-order Laue-zone ring within the dark-field detector. Because silicon has a three-layer stacking sequence *ABCABCABC*..., the natural decomposition of the 9·4 Å repeat distance into three 3·1 Å slices was chosen. Further refinement is pointless since it would produce slices containing no atoms. A final slice containing a single gold adatom was also calculated. For the sake of simplicity, surface reconstruction and crystal defects were ignored. There is an indication that 94 Å (30 slices) thick silicon (111) membranes can be prepared (Lee, Silcox & Lee, 1983*a*, *b*). This crystal thickness has been used as the base case for most of the calculations presented in this paper.

Further considerations in creating the transmission functions are their size in ångströms and sampling in pixels. The calculation must have a large reciprocal-space array in Å^{-1} (which corresponds to a dense real-space sampling) in order to include high-angle scattering (large $\alpha_{\lim}$). At the same time, the reciprocal-space array must also have dense enough sampling (which corresponds to a large real-space array in Å) to describe accurately the incident-beam aberrations and the objective aperture. These conflicting requirements result in large arrays and therefore long calculation times. The final compromise was slice dimensions a_x, $b_y = 38{\cdot}4$, 39·9 Å and sampling N_x, $N_y = 256$, 256 pixels for production runs and a_x, $b_y = 53{\cdot}7$, 53·2 Å and N_x, $N_y = 512$, 512 pixels for accuracy tests, resulting in maximum scattering angles of $\alpha_{\lim} = 79$ and $\alpha_{\lim} = 117$ mrad, respectively.

A projection of the crystal structure along the beam is shown in Fig. 1. Neighboring columns of silicon atoms are spaced by 3·84 and 2·22 Å along the x and y axes, respectively. The ticks along the x axis are referred to in §§ 4 and 5 below. Throughout this paper, line scans are taken along the x and y axes, and are centered on the origin. Typical simulated STEM line

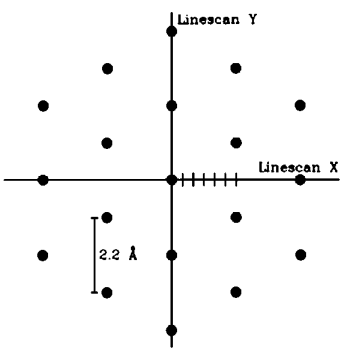

Fig. 1. The silicon crystal structure projected along the (111) axis. The circles mark the placement of columns of silicon atoms. Positions along line scan X are referred to later in the text.

scans are 20 Å long and consist of 100 points. Typical simulated STEM images are 16×16 Å in area and consist of 48×48 pixels.

The VG-HB501 STEM has the option of a low- or high-resolution pole piece for the objective lens with spherical aberrations of 3·3 and 0·7 mm respectively. Only the high-resolution pole piece is able to resolve the silicon lattice without exotic imaging methods (Kirkland *et al.*, 1987). Only the low-resolution pole piece permits tilting of the specimen in the Cornell instrument. Simulations for both pole pieces are interesting and are presented below.

The narrowest incident probe can be achieved when the objective-lens defocus balances the spherical aberration throughout the range of incident angles defined by the objective aperture. The optimal imaging condition is approximately (Scherzer, 1949)

$$\Delta f = (C_s\lambda)^{1/2} \qquad \alpha_{ap} = 2^{1/2}(\lambda/C_s)^{1/4}$$
$$d \simeq 0{\cdot}43(C_s\lambda^3)^{1/4}, \tag{14}$$

where d is the diameter at half-peak intensity of the probe at the specimen surface. For the low- and high-resolution pole pieces, this condition is achieved at $\Delta f = 1105$ Å, $\alpha_{ap} = 8{\cdot}18$ mrad, $d = 2{\cdot}7$ Å and $\Delta f = 509$ Å, $\alpha_{ap} = 12{\cdot}06$ mrad, $d = 1{\cdot}9$ Å, respectively. Other choices for defocus and objective aperture exist (Mory, Colliex & Cowley, 1987), but have not been addressed here. The effects of various choices of defocus were explored in the earlier paper (Kirkland *et al.*, 1987).

The geometry of the detector has a big impact on the information present in a STEM image. A typical annular dark-field detector may detect electrons scattered by angles between 20 mrad and many hundreds of mrad. In this simulation, any minimum and maximum angles can be chosen with the restriction that the angles cannot be larger than the usable portions of the reciprocal-space arrays (79 mrad in this case). The outer angle should be as large as possible to catch as much of the high-angle scattering, characteristic of the heavy adatom. The inner angle can include or exclude the first Bragg beams, 220 beams, from the detector depending on whether one wants to examine the silicon lattice or the heavy adatom (Kirkland *et al.*, 1987). For silicon (111) and 100 keV electrons the first Bragg beams are centered at $2\theta_{220} = 19{\cdot}3$ mrad. The two detectors shown in Fig. 2, 15–79 mrad and 30–79 mrad, were used in all STEM calculations in this paper. The inner detector includes the first Bragg beams, and the outer detector does not.

An additional consideration when choosing the detector geometry is whether to include the higher-order Laue-zone (HOLZ) rings. The intensity in the HOLZ rings comes primarily from scattering from the silicon crystal and increases with thickness. The adatom signal fluctuates with thickness (due to the channeling) but does not continually increase. Beyond some depth, the HOLZ-ring intensity will mask the adatom signal. An optimal detector for imaging an adatom on silicon (111) might extend from $2\theta_{220} + \alpha_{ap}$ to several hundred mrads and have dead zones wherever the HOLZ rings fall to suppress the silicon signal. In these calculations the HOLZ rings (which start at 88 mrad) occur at angles outside the usable portions of the reciprocal-space arrays ($\alpha_{lim} = 79$ mrad) and were not included in the detector.

4. Channeling of the electron probe

An electron probe passing through a crystal along a low-order zone axis undergoes complicated coherent elastic scattering, as described by the many-beam dynamical diffraction theory (Hirsch *et al.*, 1965; Howie, 1966; Kambe *et al.*, 1974; Buxton *et al.*, 1978). An equivalent, but more intuitive, description is that the atoms act like microlenses and focus the electron wavefunction (Ishizuka & Uyeda, 1977; Fertig & Rose, 1981). The cooperative focusing by a column

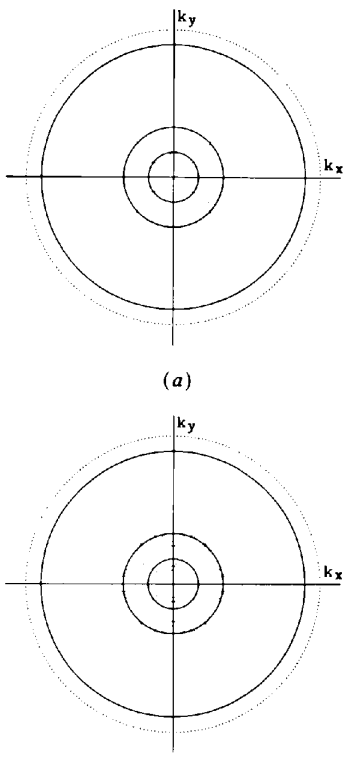

Fig. 2. The two annular dark-field detector geometries. The large solid circle marks the outer boundary for both detectors at 79 mrad. The smaller solid circles mark the inner boundary of the inner and outer detectors at 15 and 30 mrad, respectively. The large dotted circle marks the first-order Laue-zone ring at 88 mrad. The small dotted circles mark the incident beam and the first two sets of Bragg beam diffraction disks, 220 and 422. The disk radii are 8·18 mrad in (*a*), and 12·06 mrad in (*b*), corresponding to the convergence angles for the low- and high-resolution pole pieces, respectively.

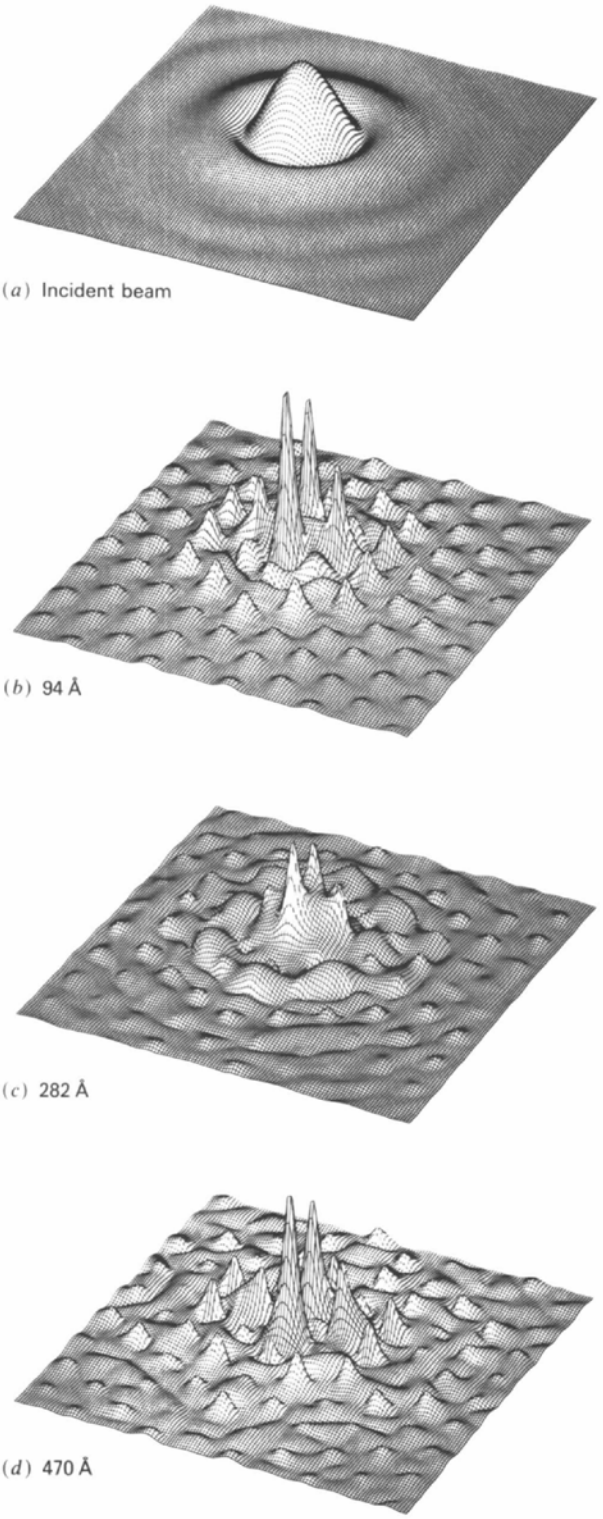

Fig. 3. The magnitude of the electron-probe wavefunction at various depths into a crystal of (111) silicon. The incident wavefunction simulated that produced by a VG-HB501 STEM (100 keV) with the low-resolution pole piece ($C_s = 3{\cdot}3$ mm, $\Delta f =$ 1105 Å, $\alpha_{ap} = 8{\cdot}18$ mrad). The incident wavefunction was randomly placed on the entrance surface of the silicon.

of atoms, called channeling, can focus a broad incident electron beam into an intense narrow peak. Such a column can behave as an optical fiber for electrons, maintaining a channeling peak and preventing beam broadening for great depths into the crystal (Fertig & Rose, 1981). A target adatom on the exit surface of the crystal should scatter more intensity if it lies under one of these channeling peaks than if it lies between. Thus channeling should have a great impact on the STEM visibility of adatoms on crystals.

An example of channeling which shows the electron-probe wavefunction magnitude at various depths (corresponding to multiples of ten sets of the three-slice stacking sequence) into a silicon crystal along the (111) axis is given in Fig. 3. Most of the electron intensity is focused into narrow channeling peaks located on the columns of silicon atoms. The ratio of the wavefunction peak to the incident peak can reach 2·5:1, which corresponds to an intensity ratio of 6:1. The ratio of the wavefunction peak to the average between peaks can reach 10:1, corresponding to an intensity ratio of 100:1! The channeling peak diameter at half-maximum intensity is ~0·7 Å. This diameter is a characteristic of the atomic potentials, and appears to be insensitive to changes in spherical aberration, defocus, objective-aperture radius, probe placement, and depth into the crystal. The channeling exhibited here is in good qualitative agreement with previous work (Fertig & Rose, 1981), although a different crystal and different algorithm have been used.

4.1. *Thickness effects on channeling*

The amount of channeling varies with depth into the crystal. Fig. 4 shows the depth dependence of the

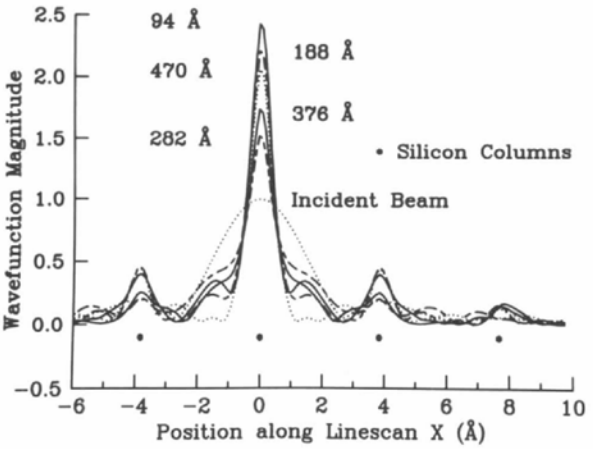

Fig. 4. The magnitude of the electron-probe wavefunction at various depths into a crystal of (111) silicon. The incident wavefunction simulated that produced by a VG-HB501 STEM (100 keV) with the low-resolution pole piece ($C_s = 3{\cdot}3$ mm, $\Delta f =$ 1105 Å, $\alpha_{ap} = 8{\cdot}18$ mrad). The incident wavefunctions were centered on a column of silicon atoms.

wavefunction for the low-resolution pole-piece probe. The depths displayed are multiples of ten sets of the three-slice stacking sequence. Within the first 94 Å of the crystal, much of the incident intensity has been focused into narrow channeling peaks. After that, the magnitudes of the channeling peaks go through maxima and minima as the electron beam propagates through the specimen. The narrower probe produced by the high-resolution pole piece (not shown here) also oscillates with the same period, but not as dramatically, possibly because the incident probe more closely matches the channeling-peak equilibrium shape. For an incident beam parallel to the silicon (111) axis, the first maximum occurs at ~100 Å. The channeling-peak intensity then oscillates with thickness with a period of ~350 Å. Even at a minimum, there is still significant channeling. Note that there is little beam broadening. Owing to the channeling, the beam width at a depth of 450 Å is almost the same as it is at 100 Å.

The periodic variation of scattered intensity with thickness is well known in CTEM (Fejes, Iijima & Cowley, 1973; Spence, O'Keefe & Kolar, 1977). The simplest two-beam 220 extinction distance for silicon is 750 Å (Hirsch, Howie, Nicholson, Pashley & Whelan, 1977), significantly larger than that observed in the channeling oscillation above. When the incident beam is along the (111) axis, the simplest dynamical calculation should include seven beams (the incident beam plus six symmetric 220 beams). The six additional beams lower the extinction distance substantially. For the (111) axis of aluminium and gold, the seven-beam extinction distance is reduced by a factor of 10·6 and 3·5, respectively, from the two-beam distances (Hirsch *et al.*, 1977). A factor of ten reduction for silicon yields an effective extinction distance of 75 Å, significantly smaller than that observed in the channeling oscillation. In STEM, the diffracted beams of CTEM are expanded into diffraction disks due to a convergent incident beam. The effective extinction distance for the STEM beam is some average between the seven-beam extinction distance, appropriate for the on-axis component of the incident beam, and the two-beam extinction distance, more appropriate for the tilted components of the incident beam. The periodic channeling behavior observed above is consistent with this picture.

4.2. *Tilt effects on channeling*

The amount of channeling produced depends on the orientation of the column of atoms with respect to the incident beam. The effects of specimen tilt (or beam tilt in the opposite direction) on channeling of the high-resolution pole-piece probe at a depth of 94 Å are shown in Fig. 5. As the tilt is increased, channeling diminishes, and the wavefunction becomes more complicated (much more complicated than is readily apparent in this 1D slice through a 2D surface). Tilting the specimen (beam) spreads out the atoms in a column perpendicular to the optical axis, which reduces their cooperative focusing and therefore reduces the channeling. Channeling falls off rapidly for tilts greater than ±4 mrad indicating that an accurate alignment of the microscope is necessary to observe channeling effects. The complicated wavefunction is a result of the highly convergent incident beam overlapping many Brillouin zones in reciprocal space, and exciting many complicated higher-order Bloch waves. At greater depths into the crystal or at higher tilts, the wavefunction becomes considerably more complicated. Very similar effects occur for the low-resolution pole-piece probe.

Further calculations indicated that if the specimen is tilted about the x axis (see Fig. 1), so that each column tilts over a nearest-neighboring column, a set of well defined channeling planes can be achieved (Howie, 1966). However, if one tilts the specimen about other axes, where columns do not overlap their nearest neighbors, the crystal specimen begins to behave as an amorphous solid and channeling disappears. Channeling is only significant while the channeling columns or planes, projected along the electron beam, are distinguishable from each other.

By tilting the specimen so that part of the convergent incident beam is at a Bragg angle, it is possible to produce intensity peaks centered between the columns of crystal atoms instead of on them. The between-column peaks, hereafter called antichanneling peaks, are not as intense or as narrow as channeling peaks. Because the probe is a convergent beam, pure channeling or pure antichanneling is not

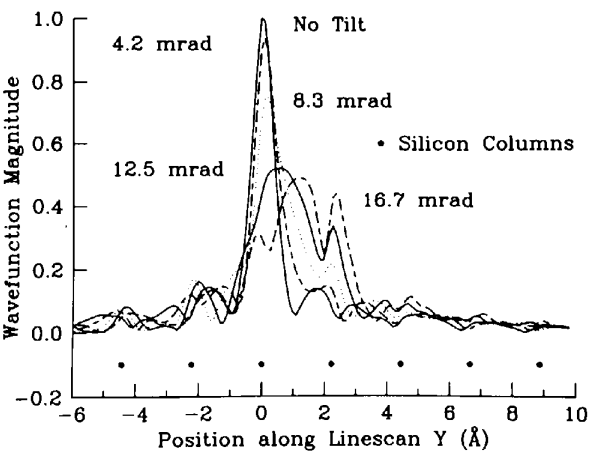

Fig. 5. The magnitude of the electron-probe wavefunction at a depth of 94 Å into a crystal of (111) silicon for various beam tilts about the x axis (in the yz plane). The angles correspond to multiples of one quarter the 422 Bragg angle. The incident wavefunction simulated that produced by a VG-HB501 STEM (100 keV) with the high-resolution pole piece ($C_s = 0{\cdot}7$ mm, $\Delta f =$ 509 Å, $\alpha_{ap} = 12{\cdot}06$ mrad). The incident wavefunctions were centered on a column of silicon atoms at the entrance surface.

expected, but rather a complicated mixture of the two. Channeling is the larger effect and usually dominates.

Little antichanneling is observed in the untilted case. This suggests a test for whether an adatom on the exit surface sits on a column or not. If the adatom becomes less visible as the specimen is tilted, it lies on the column and the decrease in channeling is responsible for the decrease in visibility. If the adatom becomes more visible as the specimen is tilted, it lies between columns and the increase in antichanneling is responsible. Tilt along different axes might further specify the adatom position.

4.3. *Probe position effects on channeling*

The intensity of a channeling peak depends on the amount of intensity that is incident on the entrance of the column. As the electron probe is scanned over a column, the intensity incident on the column rises and falls, and the height of the channeling peak rises and falls in step. A narrower probe of the same intensity puts more intensity down fewer columns, and therefore produces larger peak-to-background intensity ratios. A probe narrow enough to channel primarily down a single column of silicon atoms is narrow enough to resolve the silicon lattice in a STEM image. The high-resolution pole-piece probe is shown in Fig. 6 at a depth of 94 Å for various displacements of the probe from a column of silicon atoms. The probe positions are shown as ticks along the x axis in Fig. 1. The final position is exactly half way to the nearest-neighboring column along the x axis. At this position significant channeling occurs down columns off the x axis (not shown here). The channeling peak width, but not the peak height, remains constant regardless of the incident-probe position.

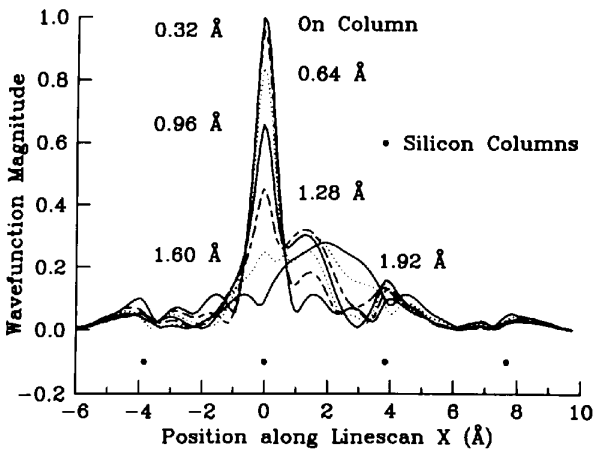

Fig. 6. The magnitude of the electron-probe wavefunction at a depth of 94 Å into a crystal of (111) silicon for various displacements of the incident beam from a column of silicon atoms. The incident wavefunction simulated that produced by a VG-HB501 STEM (100 keV) with the high-resolution pole piece (C_s = 0·7 mm, Δf = 509 Å, α_{ap} = 12·06 mrad). The probe displacements were along the x axis as shown in Fig. 1.

4.4. *Wavefunction accuracy*

Determining the accuracy of reams of output is probably the most difficult part of any major computer calculation. No matter how unsurprising or consistent the results are, one can never be sure there are no bugs in the program.

One means of monitoring the accuracy of the wavefunction is to monitor the total integrated intensity. Some intensity is lost in each slice due to high-angle scattering being removed to prevent aliasing. The total integrated intensity of the wavefunction is easily monitored at each slice and provides an estimate of the error of the calculation. For depths up to 235 Å, the integrated intensity is $\geq 90\%$ of the incident intensity. The 10% loss of intensity produced no qualitative changes in the wavefunction. Tilting the specimen lowered the amount of lost intensity, possibly by shifting parts of the higher-order Laue zones into the usable part of the reciprocal-space arrays, where they were no longer suppressed by the antialiasing.

A more direct test of the wavefunction accuracy is to compare a wavefunction to another calculated with a higher sampling. If the original sampling was sufficient, increasing it should not change the results significantly. If the results do change, the difference is a measure of the sampling error in the original calculation. It is necessary to increase the resolution in both real and reciprocal space to test adequately the sampling of the transmission functions and propagator. Throughout this investigation, production-run calculations were performed on 38·4 × 39·9 Å, 256 × 256 pixel arrays, and accuracy check calculations were performed on 53·7 × 53·2 Å, 512 × 512 pixel arrays. The two wavefunctions had a r.m.s. difference of 11%. The 512 × 512 calculations, which included the first-order Laue-zone ring in the usable portion of the reciprocal-space array, consistently lost half as much intensity as the 256 × 256 calculations. Fortunately, an 11% error in the wavefunction does not lead to an 11% error in the STEM image. Higher sampling is very expensive in this N^4 calculation, and was not possible for more than a few cases.

5. STEM visibility of single atoms

The STEM visibility of a single heavy adatom on an amorphous substrate is thought to decrease with substrate thickness, since the adatom signal is assumed constant, and the substrate signal is assumed to be linear in the number of scatterers (Crewe *et al.*, 1975; Isaacson *et al.*, 1976; Langmore, 1978). For adatoms on crystalline substrates, the large channeling effect described above may invalidate both these assumptions. In particular, for substrates $\leq$94 Å thick, the adatom signal may increase with substrate thickness due to the increasing amount of channeling. Adatom

visibility on crystal substrates may not fit conventional models, but can be estimated from STEM simulations.

Examples of simulated STEM images of a single gold adatom on 94 Å of crystalline silicon (111) are given in Fig. 7. The gold adatom was placed on the exit surface of the crystal on a column of silicon atoms, which should maximize the channeling enhancement of the adatom signal. This position is thought to occur in the gold 5×1 surface structure (Yabuuchi, Shoji, Oura & Hanawa, 1983), and has therefore been used as the base case for many of the following calculations. The two left images (Figs. 7*a* and *b*) were calculated with the low-resolution pole piece, and the right images (Figs. 7*c* and *d*) were calculated with the high-resolution pole piece. Note that the silicon lattice is not resolved with the low-resolution pole piece, but is resolved with the high-resolution pole piece. The top two images (Figs. 7*a* and *c*) were calculated with the inner detector, and the bottom two (Figs. 7*b* and *d*) were calculated with the outer detector (see Fig. 2). The gold adatom is an order of magnitude more visible in the outer detector images than in the inner detector images. Two concentric detectors with the high-resolution pole piece may be able to image the adatom and the silicon lattice simultaneously. A constant background has been subtracted from the images and the remainder has been scaled to the full gray scale. This scaling makes for better figures, but is misleading. The low-resolution inner-detector image (Fig. 7*a*) is actually almost featureless. The hexagonal pattern which is larger than the lattice spacing may be caused by reflections which are kinematically forbidden, but not dynamically forbidden. No definite conclusion can be drawn, since the magnitude of the pattern is on the order of the known error in the calculation (which is ~1% in this case).

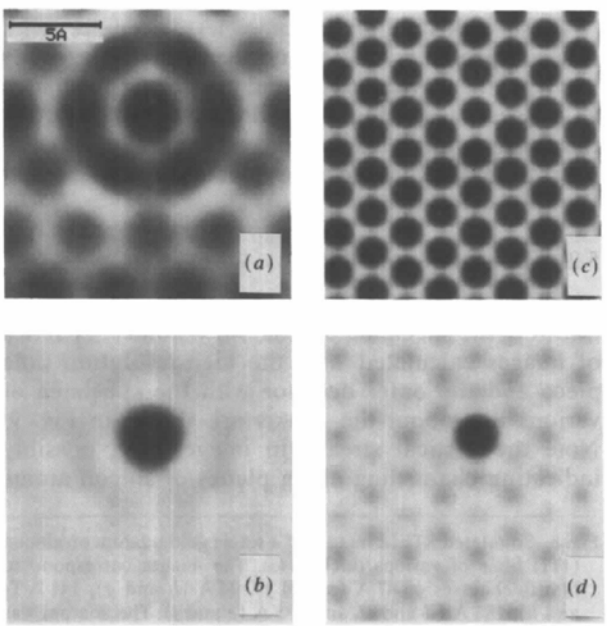

Fig. 7. Simulated VG-HB501 STEM images of a single gold adatom on a 94 Å thick silicon (111) film. The adatom was positioned on the crystal exit surface on a column of silicon atoms. Images (*a*) and (*b*) were calculated with the low-resolution pole piece ($C_s = 3{\cdot}3$ mm, $\Delta f = 1105$ Å, $\alpha_{ap} = 8{\cdot}18$ mrad), and images (*c*) and (*d*) were calculated with the high-resolution pole piece ($C_s = 0{\cdot}7$ mm, $\Delta f = 509$ Å, $\alpha_{ap} = 12{\cdot}06$ mrad). Images (*a*) and (*c*) were calculated with the inner detector (15–79 mrad), and images (*b*) and (*d*) were calculated with the outer detector (30–79 mrad). The gray scale spans the full range of intensity for each image. White represents a scattered intensity of (*a*) 0·439, (*b*) 0·0346, (*c*) 0·284, (*d*) 0·0216, and black represents an intensity of (*a*) 0·449, (*b*) 0·0611, (*c*) 0·397, (*d*) 0·0694.

The visibility of a feature in an image is dependent on noise (as discussed in § 6 below). However, when the amount of noise is sufficiently small, the visibility of a feature is proportional to its contrast. Contrast is defined as the ratio of the signal to the background, where the background is the average detected intensity, I_{av}, and the signal is the deviation from the background, $\Delta I = I - I_{av}$.

$$\text{contrast} = \Delta I / I_{av}. \tag{15}$$

An adatom will be visible in an image if its contrast is greater than some subjective constant which depends on the amount of noise.

5.1. *Thickness effects on visibility*

The first question to be addressed is how adatom visibility varies with depth. Images for both pole pieces and the outer detector for depths up to 235 Å are shown in Fig. 8. The similarity between the images at different depths is unsurprising given the channeling calculation results. Recall that within the first 94 Å much of the electron intensity is focused into the channeling peaks where it remains for at least 470 Å. The small dependence on crystal thickness of the images is an advantage of STEM over CTEM, where phase-contrast reversals can complicate image interpretation (Engel *et al.*, 1974). Values of the adatom signal, the background intensity, and the contrast for each image are listed in Table 1. These values are also listed for inner-detector images (not shown here) to demonstrate how much more visible the adatom is in the outer detector. The high-resolution pole piece produces a significantly higher contrast at all depths. Most of the contrast in the high-resolution pole-piece inner-detector images is due to the variation in the silicon-lattice signal, not the adatom signal. Note that the adatom signal and the background rise and fall as a function of depth as do the channeling peaks. The contrast does not fall off steadily for thicker specimens, and remains high up to at least 235 Å. This result is consistent with the prediction (Pennycook *et al.*, 1986) that a single bismuth atom is visible on 270 Å of silicon, even though the experimental conditions are quite different.

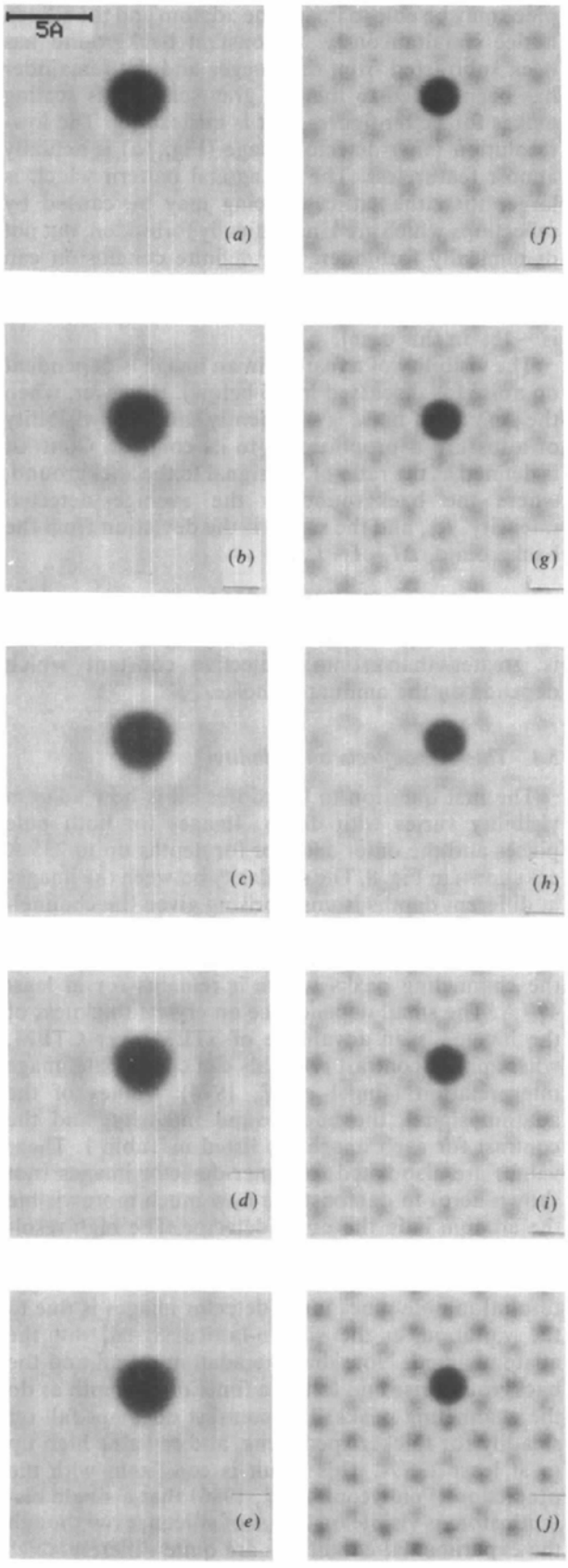

Table 1. *Thickness effects on adatom visibility; statistics for the images given in Fig.* 8

Thickness (Å)	ΔI	I_{av}	$\Delta I / I_{av}$
Low-resolution pole piece, inner detector			
47	0·0476	0·2068	0·230
94	0·0095	0·4416	0·021
141	0·0223	0·4292	0·052
188	0·0187	0·2917	0·064
235	0·0054	0·1684	0·032
Low-resolution pole piece, outer detector			
47	0·0203	0·0156	1·302
94	0·0264	0·0364	0·727
141	0·0256	0·0299	0·858
188	0·0194	0·0276	0·702
235	0·0148	0·0169	0·877
High-resolution pole piece, inner detector			
47	0·1550	0·1794	0·864
94	0·1133	0·3208	0·353
141	0·0708	0·2748	0·258
188	0·0496	0·1942	0·256
235	0·0896	0·1468	0·610
High-resolution pole piece, outer detector			
47	0·0444	0·0159	2·788
94	0·0478	0·0242	1·972
141	0·0392	0·0201	1·948
188	0·0343	0·0195	1·759
235	0·0337	0·0137	2·457

These calculations become less accurate with thicker specimens due to numerical error, intensity lost from the wavefunction, and neglected effects such as inelastic scattering. In addition, calculations for thicker specimens take an excessive amount of computer time. For these reasons, greater depths have not yet been calculated.

5.2. *Tilt effects on visibility*

Another interesting question is what are the effects of tilting the specimen on adatom visibility? A series of images calculated with the high-resolution pole piece and the outer detector with the specimen at various tilts about the x axis are shown in Fig. 9. Note the vertical streaks in images e–g, possibly indicating channeling along planes of silicon atoms

Fig. 8. Simulated STEM images of a single gold adatom on silicon (111) films of various thicknesses. The images correspond to film thicknesses of 47 Å (a and f), 94 Å (b and g), 141 Å (c and h), 188 Å (d and i), and 235 Å (e and j). The adatom was positioned on the crystal exit surface on a column of silicon atoms. The left set of images (a)-(e) was calculated with the low-resolution pole piece ($C_s = 3{\cdot}3$ mm, $\Delta f = 1105$ Å, $\alpha_{ap} = 8{\cdot}18$ mrad), and the right set (f)-(j) was calculated with the high-resolution pole piece ($C_s = 0{\cdot}7$ mm, $\Delta f = 509$ Å, $\alpha_{ap} = 12{\cdot}06$ mrad). All images were calculated with the outer detector (30–79 mrad). The gray scale spans the full range of intensity for each image. White represents a scattered intensity of (a) 0·0145, (b) 0·0346, (c) 0·0282, (d) 0·0262, (e) 0·0158, (f) 0·0137, (g) 0·0216, (h) 0·0184, (i) 0·0173, (j) 0·0112, and black represents an intensity of (a) 0·0348, (b) 0·0611, (c) 0·0538, (d) 0·0455, (e) 0·0306, (f) 0·0581, (g) 0·0694, (h) 0·0576, (i) 0·0516, (j) 0·0449. Statistics pertaining to these images are given in Table 1.

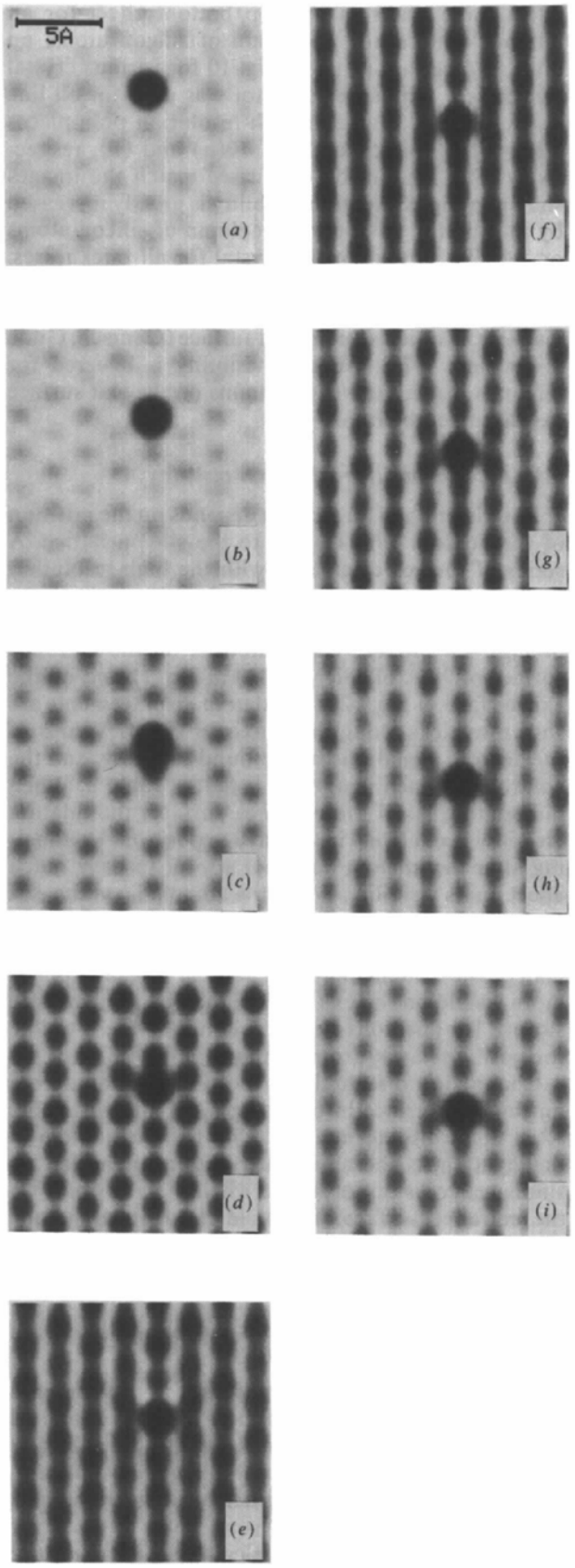

Table 2. *Tilt effects on adatom visibility; statistics for the images given in Fig. 9*

Tilt (mrad)	ΔI	I_{av}	$\Delta I/I_{av}$
	Low-resolution pole piece		
0·00	0·0264	0·0364	0·727
4·17	0·0241	0·0332	0·727
8·35	0·0140	0·0309	0·452
12·5	0·0082	0·0398	0·207
16·7	0·0094	0·0549	0·171
20·9	0·0086	0·0628	0·137
25·0	0·0117	0·0650	0·180
29·2	0·0168	0·0711	0·236
33·4	0·0192	0·0754	0·255
	High-resolution pole piece		
0·00	0·0478	0·0242	1·972
4·17	0·0421	0·0236	1·788
8·35	0·0270	0·0264	1·021
12·5	0·0226	0·0377	0·600
16·7	0·0267	0·0518	0·516
20·9	0·0246	0·0603	0·407
25·0	0·0259	0·0632	0·410
29·2	0·0318	0·0635	0·501
33·4	0·0363	0·0635	0·572

instead of columns. Values of the adatom signal, the background intensity, and the contrast for each image are listed in Table 2. These values are also listed for low-resolution pole-piece images (not shown here) for comparison purposes. These calculations show that for tilts up to ~2° tilting the specimen decreases the adatom signal, raises the background, and thus lowers the contrast. The calculations indicate that an alignment accuracy to within ±4 mrad of the silicon (111) zone axis is necessary for the channeling contrast enhancement. Similar effects occur for tilts about the y axis, but in this case, channeling planes are not observed. The change in contrast due to tilt does not appear to be sensitive to the tilt direction.

The test for adatom position described in § 4.2 was simulated with the high-resolution pole piece and the outer detector. As predicted, the contrast of an adatom located between columns increased as the specimen was tilted, due to the increase in antichanneling. As the crystal was tilted, the contrast increased to a maximum of ~1, considerably smaller than the

Fig. 9. Simulated STEM images of a single gold adatom on a 94 Å thick silicon (111) film for various specimen tilts about the x axis. The images correspond to tilts of (*a*) 0·0 mrad, (*b*) 4·2 mrad, (*c*) 8·3 mrad, (*d*) 12·5 mrad, (*e*) 16·7 mrad, (*f*) 20·9 mrad, (*g*) 25·0 mrad, (*h*) 29·2 mrad, and (*i*) 33·4 mrad. The adatom was positioned on the crystal exit surface on a column of silicon atoms. The angles correspond to multiples of one quarter the 422 Bragg angle. The images were calculated with the high-resolution pole piece ($C_s = 0{\cdot}7$ mm, $\Delta f = 509$ Å, $\alpha_{ap} = 12{\cdot}06$ mrad) and the outer detector (30–79 mrad). The gray scale spans the full range of intensity for each image. White represents a scattered intensity of (*a*) 0·0216, (*b*) 0·0210, (*c*) 0·0234, (*d*) 0·0330, (*e*) 0·0451, (*f*) 0·0543, (*g*) 0·0584, (*h*) 0·0588, (*i*) 0·0589, and black represents an intensity of (*a*) 0·0694, (*b*) 0·0631, (*c*) 0·0504, (*d*) 0·0556 (*e*) 0·0718, (*f*) 0·0789, (*g*) 0·0843, (*h*) 0·0906, (*i*) 0·0950. Statistics pertaining to these images are given in Table 2.

~2 for the untilted on-column case, but possibly still visible.

5.3. *Top/bottom effects on visibility*

A good example of the effect of channeling is exhibited by comparing images where the target adatom is on the entrance surface of the sample with those where it is on the exit surface. An adatom on the entrance surface scatters whatever intensity is incident on it from the probe. An adatom on the exit surface under a column of atoms scatters the intensity channeled down to it by the column. The difference between the two cases is the visibility enhancement (reduction) caused by channeling, *i.e.* the top/bottom effect. Line scans of the top/bottom effect for an adatom centered on a column of silicon atoms on both surfaces are given in Fig. 10 for various crystal thicknesses. The outer detector was used for all line scans, and the low- and high-resolution pole pieces were used to calculate Figs. 10(*a*) and (*b*), respectively. The adatom on exit cases match the images shown in Fig. 8. Adatom visibility is greatly increased by placing the adatom on a column of silicon atoms on the exit surface of the crystal for all thicknesses. This result is contrary to previously reported results where beam broadening in the substrate reduced the visibility of objects on the exit surface (Gentsch, Gilde & Reimer, 1973). Adatom visibility is lowered for adatoms placed between columns on the exit surface (as discussed below).

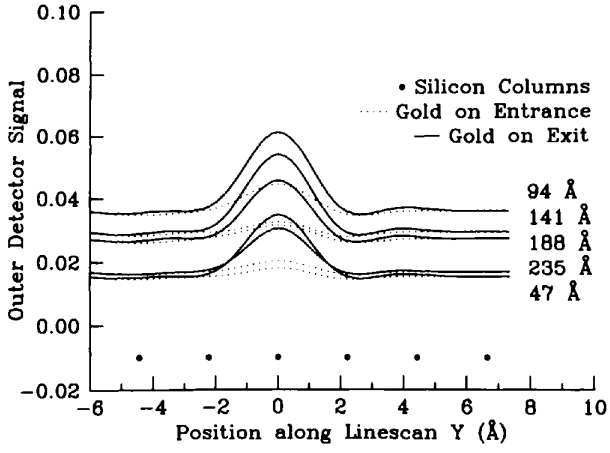

(*a*)

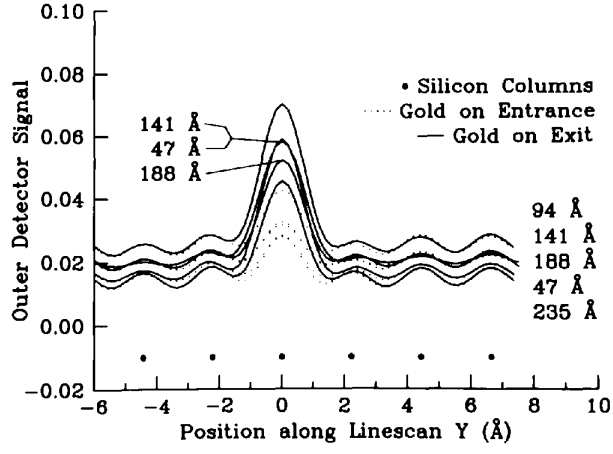

(*b*)

Fig. 10. Simulated STEM line scans of a single gold adatom on both surfaces of silicon (111) films of various thicknesses. The adatom was positioned on a column of silicon atoms. (*a*) was calculated with the low-resolution pole piece ($C_s = 3{\cdot}3$ mm, $\Delta f =$ 1105 Å, $\alpha_{ap} = 8{\cdot}18$ mrad), and (*b*) was calculated with the high-resolution pole piece ($C_s = 0{\cdot}7$ mm, $\Delta f = 509$ Å, $\alpha_{ap} =$ 12·06 mrad). Both figures were calculated with the outer detector (30–79 mrad).

5.4. *Adatom position effects on visibility*

The visibility of an adatom depends on the position of the adatom with respect to the silicon lattice. A series of images calculated with the high-resolution pole piece and the outer detector for various displacements of the gold adatom from a column are shown in Figs. 11 and 12. The adatom is on the entrance surface of 94 Å of silicon (111) in Fig. 11 and on the exit surface in Fig. 12. The adatom displacements are shown as ticks along the x axis in Fig. 1. Values of the adatom signal, the background intensity, and the contrast for each image are listed in Table 3. When the adatom is on the entrance surface, the adatom visibility is relatively insensitive to position. Channeling after the adatom does not appear to have much effect on its visibility. When the adatom is on the exit surface, the visibility falls off dramatically for displacements larger than ~0·4 Å, which is approximately the channeling-peak radius. The adatom is more visible on the exit surface than on the entrance surface for positions near a column, and less visible for positions away from columns.

Channeling distorted the location of the adatom on the exit surface in the images. As shown in Fig. 12, a slight displacement (<0·8 Å) of the adatom to the right shifts the apparent position to the left. A similar effect is not observed when the adatom is on the entrance surface. To avoid the distortion, one must sacrifice the visibility enhancement produced by channeling, and put the adatom on the entrance surface.

5.5. *STEM calculation accuracy*

The primary test of image accuracy was to compare an image calculated on 38·4×39·9 Å, 256×256 pixel arrays to one calculated on 53·7×53·2 Å, 512×512 pixel arrays. If the original sampling was sufficient, increasing the sampling should not change the results. The result of these comparisons was a r.m.s. error estimate of 1% for images calculated with the inner

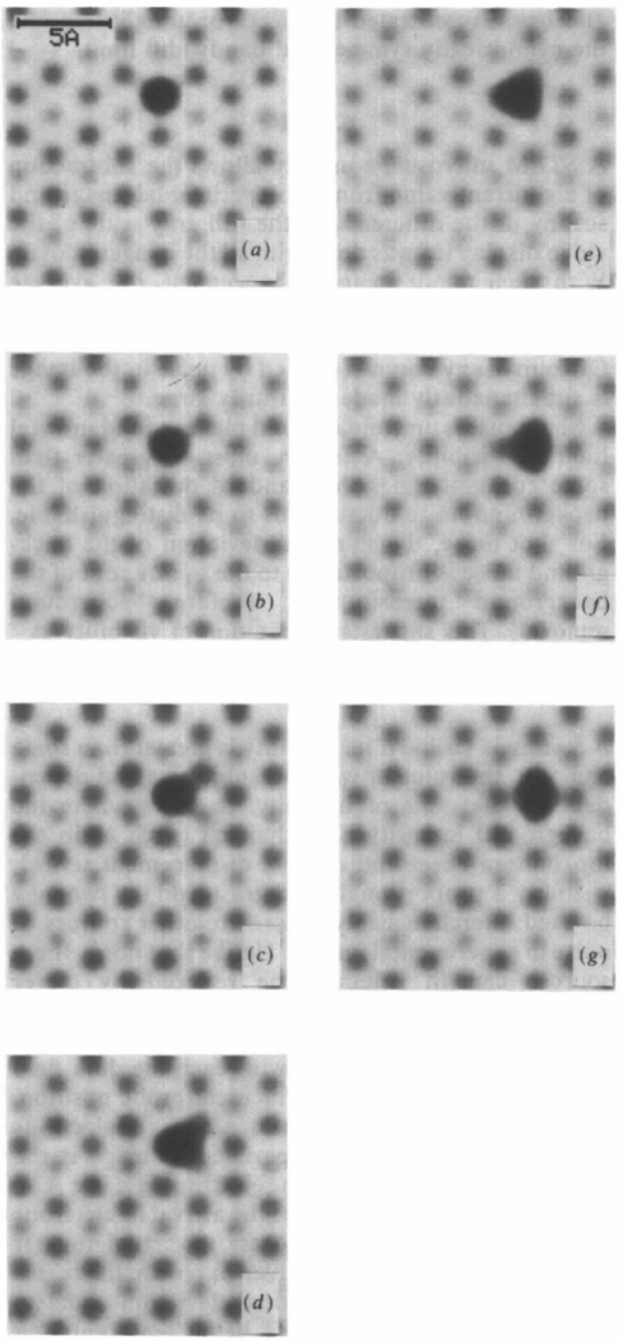

Fig. 11. Simulated STEM images of a single gold adatom on a 94 Å thick silicon (111) film for various displacements of the adatom on the entrance surface. The images correspond to displacements of (*a*) 0·0 Å, (*b*) 0·32 Å, (*c*) 0·64 Å, (*d*) 0·96 Å, (*e*) 1·28 Å, (*f*) 1·60 Å, and (*g*) 1·92 Å along the *x* axis as shown in Fig. 1. The images were calculated with the high-resolution pole piece ($C_s = 0{\cdot}7$ mm, $\Delta f = 509$ Å, $\alpha_{ap} = 12{\cdot}06$ mrad) and the outer detector (30–79 mrad). The gray scale spans the full range of intensity for each image. White represents a scattered intensity of 0·0216 in all images. Black represents an intensity of (*a*) 0·0422, (*b*) 0·0454, (*c*) 0·0421, (*d*) 0·0452, (*e*) 0·0476, (*f*) 0·0465, (*g*) 0·0453. Statistics pertaining to these images are given in Table 3.

detector and 6% for images calculated with the outer detector. This error was approximately thickness independent, tilt independent, and pole-piece independent. Note that a line scan is just a one-pixel-wide image, so the same test and results apply to both.

This thickness-independent error estimate does not match the thickness-dependent loss of intensity from the electron wavefunction. The explanation of this

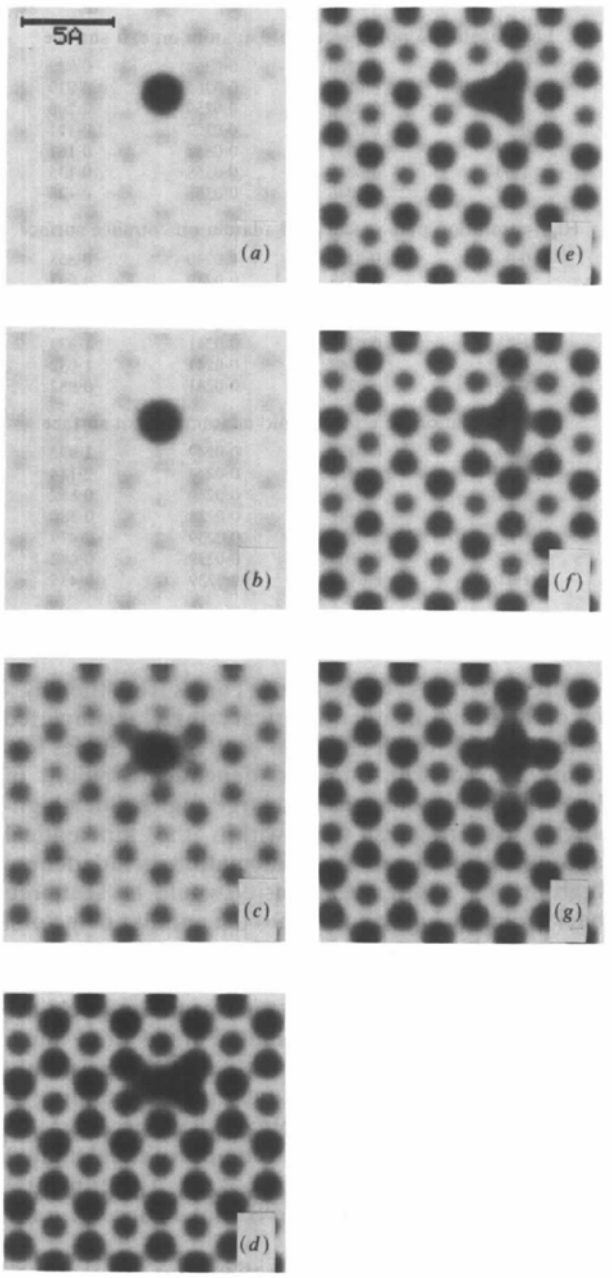

Fig. 12. As Fig. 11 except the gold adatom was on the exit surface. White represents a scattered intensity of 0·0216 in all images. Black represents an intensity of (*a*) 0·0694, (*b*) 0·0730, (*c*) 0·0422, (*d*) 0·0307, (*e*) 0·0330, (*f*) 0·0322, (*g*) 0·0320.

Table 3. *Adatom offset effects on adatom visibility; statistics for the images given in Figs.* 11 *and* 12

Offset (Å)	ΔI	I_{av}	$\Delta I/I_{av}$
Low-resolution pole piece, gold adatom on entrance surface			
0·00	0·0098	0·0359	0·273
0·32	0·0108	0·0359	0·300
0·64	0·0085	0·0359	0·238
0·96	0·0119	0·0360	0·331
1·28	0·0147	0·0360	0·408
1·60	0·0126	0·0360	0·349
1·92	0·0107	0·0360	0·297
Low-resolution pole piece, gold adatom on exit surface			
0·00	0·0264	0·0364	0·727
0·32	0·0295	0·0365	0·810
0·64	0·0096	0·0359	0·266
0·96	0·0043	0·0357	0·121
1·28	0·0057	0·0358	0·161
1·60	0·0048	0·0358	0·135
1·92	0·0046	0·0358	0·128
High-resolution pole piece, gold adatom on entrance surface			
0·00	0·0205	0·0240	0·858
0·32	0·0238	0·0240	0·993
0·64	0·0205	0·0240	0·855
0·96	0·0235	0·0240	0·982
1·28	0·0260	0·0241	1·079
1·60	0·0249	0·0241	1·032
1·92	0·0236	0·0241	0·982
High-resolution pole piece, gold adatom on exit surface			
0·00	0·0478	0·0242	1·972
0·32	0·0514	0·0243	2·114
0·64	0·0207	0·0240	0·862
0·96	0·0091	0·0238	0·380
1·28	0·0115	0·0239	0·479
1·60	0·0106	0·0239	0·442
1·92	0·0104	0·0239	0·435

difference in the error estimates comes from the physics of the situation, not numerical error. Our simulated detectors only catch electrons scattered at angles less than 79 mrad. The thickness-dependent amount of lost intensity is scattered into large angles. Such high-angle scattering is well within the kinematical approximation. Even if our calculation included these high angles, negligible intensity would be scattered back from the high angles onto the annular detectors. Accuracy tests that included larger-angle scattering supported this claim.

Most of the accuracy checks performed were checks for self consistency. Systematic errors are much harder to find. A factor of two error, consistently included in all the scattering factors, or something of that nature, might go unnoticed. The best test for absolute accuracy would be to compare the calculated images to experimental images. Experimental confirmation of the simulated STEM-image accuracy is currently being pursued.

A final check was applied to all images. Any sources of unphysical features in the image were tracked down and eliminated. For example, horizontal streaks in a supposedly hexagonally symmetric image are definitely an error. This check has been very effective, and has demonstrated the need for antialiasing and the cylindrically symmetrical bandwidth limit.

6. Noise

A STEM microscope usually allows the subtraction of a constant value from an experimental image and scaling of the difference to the full gray scale of the video display (as was done with all the images above). With such minor image enhancement, the average background can be set to zero and the contrast, by the previous definition, can be made arbitrarily large. Of course, any contrast caused by noise in the image is simultaneously made arbitrarily large.

Shot noise is unavoidable and places a fundamental limit on visibility. A feature must be greater than some constant times the standard deviation of the background-noise fluctuations to be distinguishable. For shot noise, the standard deviation of the background noise is proportional to the square root of the background intensity, I_{av} (before background removal). This suggests a definition of visibility as

$$\text{visibility} = \Delta I/(I_{av})^{1/2} = \text{contrast } (I_{av})^{1/2}. \quad (16)$$

A feature is visible if its visibility is greater than some constant, the value of which is subjective and dependent on the units of intensity. In cases where the background intensity is unchanged (such as in the top/bottom effect and adatom displacement series), visibility is proportional to contrast, and the two may be used interchangeably. There are other sources of noise in experimental images. Unlike shot noise, these sources can in principle be reduced by clever engineering, and have therefore not been considered.

The STEM image simulation produces the probability that a given electron will reach the dark-field detector as a function of the incident-probe position. In an ideal microscope, the mean number of electrons detected per pixel in an experimental image is the product of that probability, the electron dose in e $Å^{-2}$, and the pixel area in $Å^2$. Since the arrival of electrons at the detector is a Poisson process, the actual number of electrons that arrive in a given exposure fluctuates about the mean with a standard deviation equal to the square root of the mean. A better representation of experimental images is possible by replacing each pixel in the simulated images with a Poisson random deviate with the same mean as the mean number of electrons expected in that pixel.

A program was written to add shot noise to the simulated images. The subroutines for generating Poisson random deviates were taken from *Numerical Recipes* (Press, Flannery, Teukolsky & Vetterling, 1986). Several sets of 10 000 random deviates with different means were calculated and examined as a program accuracy test. The test sets of deviates had the correct means, standard deviations, and

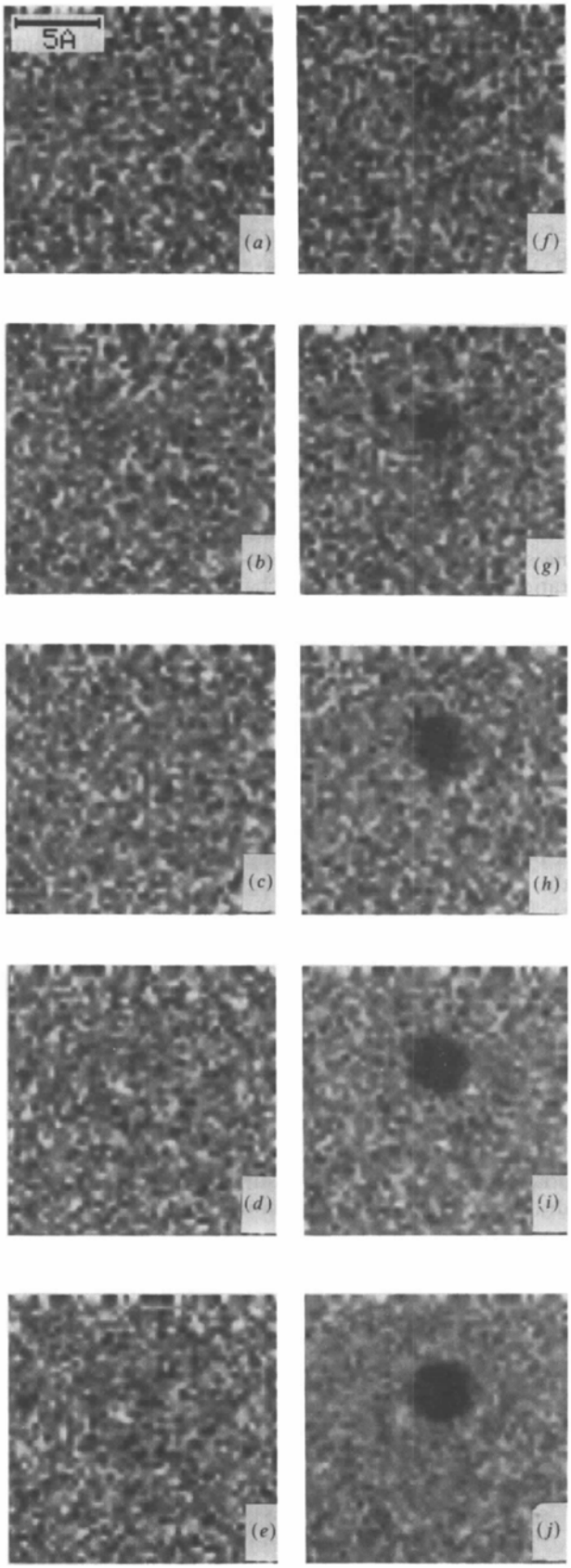

Table 4. *Dose effects on adatom visibility; statistics for the images given in Figs.* 13 *and* 14

Dose (e Å^{-2})	ΔI	I_{av}	$\Delta I/I_{av}$	$\Delta I/(I_{av})^{1/2}$
Low-resolution pole piece, inner detector				
1×10^3	457	442	1·034	21·75
3×10^3	794	1326	0·599	21·80
1×10^4	1389	4420	0·314	20·90
3×10^4	2338	13254	0·176	20·31
1×10^5	4211	44187	0·095	20·03
Low-resolution pole piece, outer detector				
1×10^3	138	37	3·758	22·78
3×10^3	250	110	2·280	23·98
1×10^4	621	364	1·708	32·57
3×10^4	1251	1092	1·146	37·87
1×10^5	3340	3640	0·934	56·35
High-resolution pole piece, inner detector				
1×10^3	414	321	1·290	23·12
3×10^3	811	962	0·843	26·15
1×10^4	1795	3212	0·559	31·67
3×10^4	4263	9634	0·442	43·43
1×10^5	12926	32099	0·403	72·15
High-resolution pole piece, outer detector				
1×10^3	95	24	3·885	19·20
3×10^3	233	73	3·191	27·27
1×10^4	630	243	2·597	40·44
3×10^4	1898	728	2·607	70·35
1×10^5	5100	2427	2·102	103·5

distributions to within the expected error caused by finite sampling.

Shot noise has been added to the images in Fig. 7 for doses of 10^3 to 10^5 eÅ^{-2}. The left and right sets of images in Fig. 13 correspond to the simulated images Figs. 7(*a*) and (*b*), respectively. The left and right sets of images in Fig. 14 correspond to the simulated images Figs. 7(*c*) and (*d*), respectively. Table 4 lists the corresponding adatom signals, backgrounds, contrasts, and visibilities. The image gray scales have been normalized to span ±3 standard deviations about the image mean. Even without image processing, the adatom is plainly visible. As mentioned above, the inner-detector low-resolution pole-piece image is featureless, and the adatom is an order of magnitude more visible with the outer detector.

The higher the dose, the less relative noise in the image, provided the specimen can withstand the bombardment by high-energy electrons. Because silicon is a tough substance (strong covalent bonds), the main

Fig. 13. Shot noise added to the simulated STEM images shown in Fig. 7. The left set of images (*a*)-(*e*) was calculated from image 7(*a*) and the right set (*f*)-(*j*) was calculated from image 7(*b*). The images correspond to doses of 1×10^3 e Å^{-2} (*a* and *f*), 3×10^3 e Å^{-2} (*b* and *g*), 1×10^4 e Å^{-2} (*c* and *h*), 3×10^4 e Å^{-2} (*d* and *i*), and 1×10^5 e Å^{-2} (*e* and *j*). The gray scales have been scaled to ±3 standard deviations of the intensity variation in the image. White represents a scattered intensity in e Å^{-2} of (*a*) 258, (*b*) 1010, (*c*) 3836, (*d*) 12238, (*e*) 42276, (*f*) −18, (*g*) 15, (*h*) 176, (*i*) 709, (*j*) 2662, and black represents an intensity of (*a*) 626, (*b*) 1642, (*c*) 5005, (*d*) 14 269, (*e*) 46 089, (*f*) 91, (*g*) 205, (*h*) 551, (*i*) 1475, (*j*) 4619. Statistics pertaining to these images are given in Table 4.

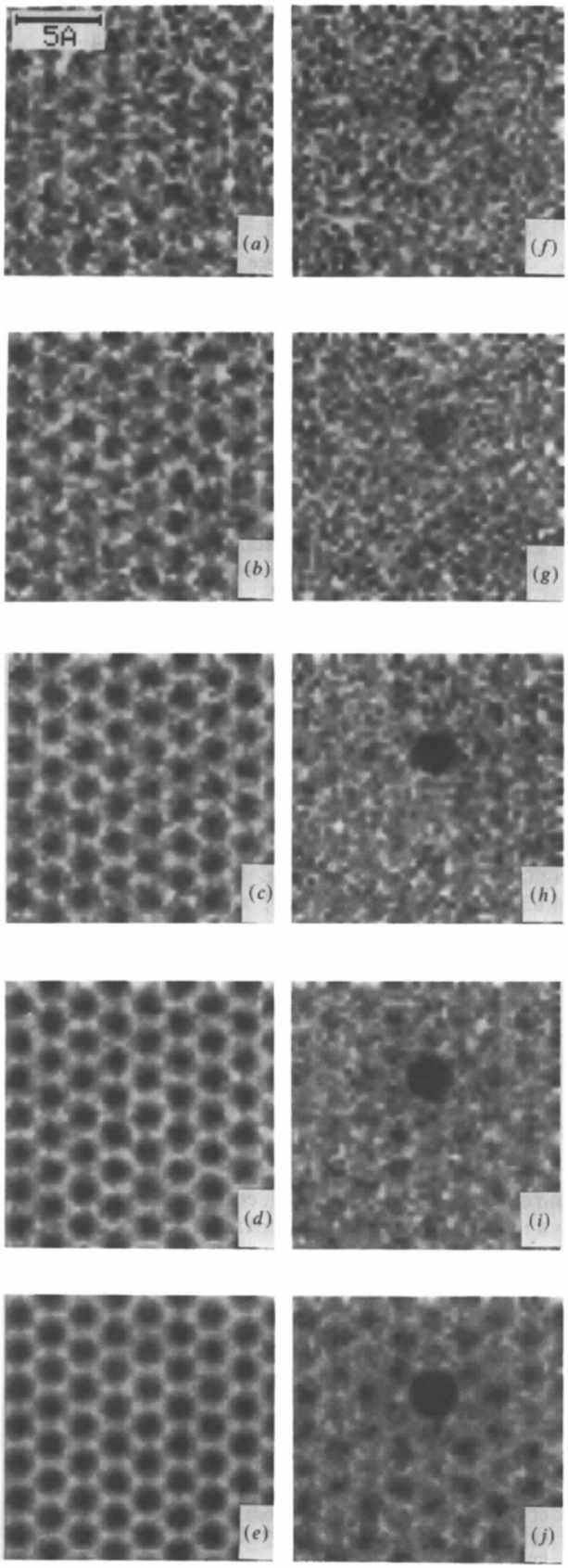

damage of concern is displacing the heavy adatom. Noisy images have been calculated at several different doses since the critical dose necessary to desorb a heavy adatom is not known.

7. Concluding remarks

The images simulated for this paper suggest a number of interesting effects that may be visible in ADF STEM images of single heavy atoms on crystalline substrates. There is a strong correlation between the amount of channeling in the silicon crystal and the visibility of an adatom on its surface. Due to channeling, single gold adatoms should be visible on the exit surface of silicon (111) crystals for thicknesses of at least 235 Å.

Channeling is a big effect along low-order axes, and should not be ignored. Channeling peaks for 100 keV electrons along silicon (111) are 0·7 Å wide independent of beam parameters and specimen thickness. The channeling peak-to-background intensity ratios can reach 100:1. The channeling peak intensity oscillates with depth into the crystal. Specimen tilt decreases the amount of channeling, independent of tilt direction. A beam alignment to within ±4 mrad is necessary to produce significant channeling. Channeling is maximized by centering the incident probe on a column of atoms.

The annular dark-field STEM visibility of an adatom is directly related to channeling. The more intensity channeled to the adatom, the larger signal it produces. As the channeling oscillates with depth, the signal produced by a single adatom on the exit surface and the signal from the silicon substrate also oscillate, but the ratio of the two signals stays roughly constant. These simulations indicate that film thickness is not as crucial to single-atom imaging on crystalline substrates as one would expect, because channeling prevents beam broadening. Tilt of the specimen reduces channeling, and therefore adatom visibility. Channeling effects are absent when the adatom is on the entrance surface, and the signal is correspondingly lower. The adatom signal is very dependent on adatom position on the exit surface. The signal drops dramatically when the adatom is moved out from under a channeling peak.

The annular detector geometry is crucial for visibility. For a single adatom to be visible, the silicon substrate signal must be minimized by excluding low-order Bragg beams from the detector. With the high-resolution pole piece and two concentric detectors,

Fig. 14. As Fig. 13 except noise was added to images Figs. 7(*c*) and 7(*d*). White represents a scattered intensity in e $Å^{-2}$ of (*a*) 142, (*b*) 595, (*c*) 2214, (*d*) 6912, (*e*) 23 355, (*f*) −21, (*g*) −9, (*h*) 66, (*i*) 309, (*j*) 1233, and black represents an intensity of (*a*) 500, (*b*) 1330, (*c*) 4211, (*d*) 12 355, (*e*) 40 843, (*f*) 69, (*g*) 155, (*h*) 419, (*i*) 1147, (*j*) 3620. Statistics pertaining to these images are given in Table 4.

it should be possible to resolve the adatom and the silicon lattice simultaneously.

Since only intensity scattered at relatively high angles falls on the detector, the adatom signal as a function of adatom atomic number is proportional to something between $Z^{3/2}$ to Z^2. The high visibility of gold indicates single atoms of all the $5d$ heavy transition metals should be visible.

This work was supported by the Department of Energy (grant no. DE-FG02-87ER45322). It made use of the Cornell National Supercomputer Facility, a resource of the Center for Theory and Simulation in Science and Engineering at Cornell University, which is funded in part by the National Science Foundation, New York State, and the IBM Corporation. The computer programs used in this work were developed earlier under support from the NSF (grant no. ECS-8516867) and the Materials Science Center at Cornell (NSF grant no. DMR 8516616).

References

BUXTON, B. F., LOVELUCK, J. E. & STEEDS, J. W. (1978). *Philos. Mag.* A**38**, 259-278.

COWLEY, J. M. (1973). *Acta Cryst.* A**29**, 529-536.

COWLEY, J. M. (1976). *Ultramicroscopy*, **2**, 3-16.

COWLEY, J. M. & MOODIE, A. F. (1957). *Acta Cryst.* **10**, 609-619.

COWLEY, J. M. & SPENCE, J. C. H. (1979). *Ultramicroscopy*, **3**, 433-438.

CREWE, A. V., LANGMORE, J. P. & ISAACSON, M. S. (1975). *Physical Aspects of Electron Microscopy and Microbeam Analysis*, edited by B. M. SIEGEL & D. K. BEAMAN, pp. 47-62. New York: Wiley.

DONALD, A. M. & CRAVEN, A. J. (1979). *Philos. Mag.* A**39**, 1-11.

ENGEL, A., WIGGINS, J. W. & WOODRUFF, D. C. (1974). *J. Appl. Phys.* **45**, 2739-2747.

FEJES, P. L., IIJIMA, S. & COWLEY, J. M. (1973). *Acta Cryst.* A**29**, 710-714.

FERTIG, J. & ROSE, H. (1981). *Optik (Stuttgart)*, **59**, 407-429.

GENTSCH, P., GILDE, H. & REIMER, L. (1974). *J. Microsc.* **100**, 81-92.

GOODMAN, P. & MOODIE, A. F. (1974). *Acta Cryst.* A**30**, 280-290.

HIRSCH, P. B., HOWIE, A., NICHOLSON, R. B., PASHLEY, D. W. & WHELAN, M. J. (1965). *Electron Microscopy of Thin Crystals*, pp. 215-217. Washington, DC: Butterworth.

HIRSCH, P. B., HOWIE, A., NICHOLSON, R. B., PASHLEY, D. W. & WHELAN, M. J. (1977). *Electron Microscopy of Thin Crystals*, pp. 285-286, 510-511. Malabar: Robert E. Krieger.

HOWIE, A. (1966). *Philos. Mag.* **14**, 223-237.

HOWIE, A. (1979). *J. Microsc.* **117**, 11-23.

International Tables for X-ray Crystallography (1974). Vol. IV, pp. 99-101. Birmingham: Kynoch Press. (Present distributor Kluwer Academic Publishers, Dordrecht.)

ISAACSON, M. S., LANGMORE, J. P., PARKER, N. W., KOPF, D. & UTLAUT, M. (1976). *Ultramicroscopy*, **1**, 359-376.

ISHIZUKA, K. & UYEDA, N. (1977). *Acta Cryst.* A**33**, 740-749.

KAMBE, K., LEHMPFUHL, G. & FUJIMOTO, F. (1974). *Z. Naturforsch. Teil A*, **29**, 1034-1044.

KIRKLAND, E. J., LOANE, R. F. & SILCOX, J. (1987). *Ultramicroscopy*, **23**, 77-96.

LANGMORE, J. P. (1978). *Principles and Techniques of Electron Microscopy*, Vol. 9, edited by M. A. HAYAT, pp. 1-63. New York: Van Nostrand Reinhold.

LEE, K. C., SILCOX, J. & LEE, C. A. (1983*a*). *J. Appl. Phys.* **54**, 4035-4037.

LEE, K. C., SILCOX, J. & LEE, C. A. (1983*b*). *Appl. Phys. Lett.* **43**, 488-489.

MORY, C., COLLIEX, C. & COWLEY, J. M. (1987). *Ultramicroscopy*, **21**, 171-178.

O'KEEFE, M. A. & BUSECK, P. R. (1979). *Trans. Am. Crystallogr. Assoc.* **15**, 27-46.

PENG, L.-M. & COWLEY, J. M. (1988). *Acta Cryst.* A**44**, 1-5.

PENNYCOOK, S. J., BERGER, S. D. & CULBERTSON, R. J. (1986). *J. Microsc.* **144**, 229-249.

PENNYCOOK, S. J. & NARAYAN, J. (1985). *Phys. Rev. Lett.* **54**, 1543-1546.

PRESS, W. H., FLANNERY, B. P., TEUKOLSKY, S. A. & VETTERLING, W. T. (1986). *Numerical Recipes*, pp. 191-208. Cambridge Univ. Press.

SCHERZER, O. (1949). *J. Appl. Phys.* **20**, 20-29.

SELF, P. G., O'KEEFE, M. A., BUSECK, P. R. & SPARGO, A. E. C. (1983). *Ultramicroscopy*, **11**, 35-52.

SPENCE, J. C. H., O'KEEFE, M. A. & KOLAR, H. (1977). *Optik (Stuttgart)*, **49**, 307-323.

SPENCE, J. C. H. & TAFTO, J. (1983). *J. Microsc.* **130**, 147-154.

TREACY, M. M. J. (1981). *Scanning Electron Microscopy*, Vol. 1, edited by O. JOHARI, pp. 185-197. Chicago: SEM Inc.

VAN DYCK, D. (1985). *Advances in Electronics and Electron Physics*, Vol. 65, edited by P. HAWKES, pp. 295-355. Orlando: Academic Press.

YABUUCHI, Y., SHOJI, F., OURA, K. & HANAWA, T. (1983). *Surface Sci.* **131**, L412-L418.